Engineering Fracture Mechanics 320 (2025) 111011

Contents lists available at ScienceDirect

Engineering Fracture Mechanics

journal homepage: www.elsevier.com/locate/engfracmech

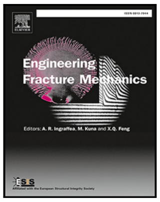

Fracture characterization of ductile polymer cellular model structures manufactured by FDM

Jacopo Agnelli [a], Claudia Pagano [b], Irene Fassi [b], Luca D'Andrea [c], Pasquale Vena [c], Laura Treccani [d], Fabio Bignotti [a], Francesco Baldi [a],*

[a] Università degli Studi di Brescia, Department of Mechanical and Industrial Engineering, Via Branze 38, I - 25123 Brescia, Italy
[b] STIIMA-CNR, Institute of Intelligent Industrial Systems and Technologies for Advanced Manufacturing, Consiglio Nazionale delle Ricerche, Via A. Corti 12, I - 20133 Milano, Italy
[c] Politecnico di Milano, Department of Chemistry, Materials and Chemical Engineering "Giulio Natta" - Laboratory of Biological Structure Mechanics (LaBS), Piazza Leonardo da Vinci 32, I - 20133, Milano, Italy
[d] CSMT Gestione S.c.a.r.l., Via Branze 45, I - 25123 Brescia, Italy

ARTICLE INFO

Keywords:
ABS
Additive manufacturing
FDM
Cellular solids
Fracture toughness
J-integral

ABSTRACT

This work addresses specific fundamental and methodological issues regarding the applicability of Fracture Mechanics (FM) testing schemes to polymer open-celled cellular solids with controlled architecture, exhibiting an elastic–plastic response and with pronounced structural heterogeneity at the cell-scale. Acrylonitrile-Butadiene-Styrene (ABS) model structures were manufactured by Fused Deposition Modeling (FDM), and their mode-I fracture response investigated. Structures with different porosity degrees (from ≈ 20% to ≈ 70%) were examined, and initiation fracture toughness (J-integral) data determined. Different modes of mechanical macro-confinement experienced by the circular cross-section beam-like structural element were noticed, able to drive a transition from true cellular to solid containing isolated pores.

1. Introduction

The technological opportunities offered by 3D printing techniques of polymeric materials [1,2], coupled with a growing demand for highly reliable and lightweight materials and structures from many industries (such as automotive [3,4], aerospace [5], sports [6] and biomedical [7]), are driving an increasing interest in the use of polymer open-celled cellular solids for structural applications. Within the class of open-celled cellular solids [8], of particular interest for designing purposes are those of architected type (often referred to as lattice structures, when made of structs and nodes), which exhibit a more *a priori* controllable structure and, consequently, programmable performances, with respect to stochastic foams (see, for example [9–11]).

It is known that, for the design of structural components, knowledge of the structural integrity characteristics of candidate materials plays a crucial role and, with reference to this, Fracture Mechanics, FM, certainly offers the most complete and appropriate framework for an exhaustive description of the material behavior [12]. Concerning polymer lattice structures, even if their mechanical response and failure mechanisms have been the object of several studies (see, for example [13–15]), at the authors' knowledge, only a few works addressed their macroscopic response under the framework of FM [16,17].

In this work, we intend to address specific fundamental and methodological issues concerning the applicability of FM testing schemes to the fracture characterization of polymer open-celled cellular solids with controlled architecture. To consider the

---

* Corresponding author.
E-mail address: francesco.baldi@unibs.it (F. Baldi).

https://doi.org/10.1016/j.engfracmech.2025.111011
Received 1 October 2024; Accepted 2 March 2025

Nomenclature

Abbreviations

ABS	Acrylonitrile-Butadiene-Styrene
CAD	Computer-Aided Design
FDM	Fused Deposition Modeling
FM	Fracture Mechanics
SE(B)	Single-Edge notched in Bending
STL	Standard Triangulation Language

Symbols

$\alpha = \mathrm{a}_0/\mathrm{W}$	Initial crack length to width ratio
$\bar{e}$	Equivalent plastic strain
$\Delta \mathrm{X}$	Width of the region used for the contact point evaluation (= 2d)
$\underline{\underline{\dot{\varepsilon}}}^{p}$	Incremental plastic strain tensor
$\dot{\varepsilon}$	Strain rate
$\mathbb{N}$	Natural numbers set
$\varphi(\alpha)$	Adimensional geometry-dependent coefficient
φ_{p}	Actual porosity degree
ν	Poisson's ratio
ρ_{ABS}	Density of ABS filament
ρ_{app}	Apparent (structure) density
ρ_{rel}	Relative (structure) density
a_0	Initial crack length
$\mathrm{a}_{0,\mathrm{n}}$	Nominal initial crack length
B	Specimen thickness
C_0	Initial elastic compliance corrected from indentation effects
D	In-plane separation between adjacent filament windings
d	Filament diameter
E	Young's modulus
E_{f}	Index of structure elastic stiffness
$\mathrm{f}(\alpha)$	Adimensional geometry-dependent coefficient
$\mathrm{J}_{\mathrm{c,i,mean}}$	Mean of the $\mathrm{J}_{\mathrm{c,i}}$ mean values for porosity levels between 35% and 73%
$\mathrm{J}_{\mathrm{c,i}}$	Initiation fracture toughness
L	Specimen length
n	Power-law exponent
$\mathrm{N}_{\mathrm{cp},0^{\circ}45^{\circ}}$	Number of contact points between 0° and +45° layers within ΔX
$\mathrm{N}_{\mathrm{f,notch}}$	Number of filaments constituting the crack front
P	Load
R	Curvature radii of in-plane filament windings
S	Span
Type A	SE(B) specimen type characterized by 3D-printed notch
Type B	SE(B) specimen type characterized by blade notch
U	Area under the P *vs.* $\mathrm{u}_{\mathrm{corr}}$ curve up to the initiation point
$\mathrm{u}_{\mathrm{corr}}$	Displacement corrected from initial transient and indentation effects
v	Crosshead speed
W	Specimen width
X	Longitudinal in-plane direction
X-notch	Position of the notch in X direction
Y	Transversal in-plane direction
Z	3D-growth direction

complications given by plasticity and by a high degree of structural complexity, attention was paid to structures with an elastic–plastic response and characterized by a pronounced degree of structural heterogeneity at the cell-scale [8]. To this aim, specific polymeric model structures were manufactured by Fused Deposition Modeling (FDM), and their fracture response investigated under mode-I loading (at macroscopic scale). The systems examined were three-dimensional open-celled structures, composed of unit cells with different shapes and dimensions manufactured to form regularly repeating patterns, in a ductile polymer (an Acrylonitrile-Butadiene-Styrene, ABS, resin). The design was based on a circular cross-section beam-like element (with diameter of ≈ 0.5 mm), directly formed by the filament extruded by the 3D printer under controlled conditions. For the fracture characterization, Single Edge notched in Bending, SE(B), tests were carried out on specifically manufactured bar-shaped specimens, in quasi-static conditions and at room temperature. Structures with different degrees of porosity (between ≈ 20% and ≈ 70%) were examined. The details concerning the fabrication of the structures with the highest degree of porosity, their morphological characteristics and mechanical response under compression, as well as the mechanical behavior of the polymeric element forming the 3D-structures, were previously reported in [18].

The examined structures are porous, strongly inhomogeneous, characterized by a moderately high compliance (E ≈ 70 MPa for the highest porosity degree) and made of a constituent material with a ductile response. On the basis of this, the use of an Elastic–Plastic FM energy-based parameter (J-integral), representative of the structure response at a global level, was preferred over the stress intensity factor (characteristic of the region surrounding the crack tip) to represent their fracture toughness. In consideration of the peculiar nature of these materials, in addressing FM testing, special attention was paid to: (i) specimen notching; (ii) correction tests for specimen indentation; (iii) determination of a point that could be considered representative of fracture initiation in the fracture test. Data of fracture toughness at initiation were evaluated for the different structures, and specific structure–property relationships tentatively developed.

The study was complemented with a Finite Element Modeling (FEM) simulation of a SE(B) test on a sharp-notched specimen with the highest porosity. The aim of the simulation was to provide a first description of the local failure mechanisms taking place during the fracture process, including the propagation phase, particularly in the regions hardly accessible *via* conventional optical instruments.

2. Experimental

2.1. Material and fabrication of the specimens

An Original Prusa i3 MK3S+ FDM printer, equipped with a nozzle of 0.4 mm in diameter, was used to manufacture the model structures with a commercial filament of ABS. The design of the structures was based on: (i) a continuous circular cross-section beam-like element, directly formed by the filament extruded by the FDM printer, under controlled conditions (the density of the ABS filament, ρ_{ABS}, is 1.06 g/cm^3); (ii) a layer-by-layer architecture built on the repetition of a ordered 4-layer basic unit with filament deposition direction different from layer to layer. The details about material, FDM printing conditions, filament properties and structure architecture are reported in [18].

In the present work, for the FM tests, rectangular-base prism ($B \times W \times L = 8 \times 16 \times 80$ mm^3, referring to thickness, width and length, respectively, as showed in Fig. 1(a)) was selected as a suitable specimen geometry. The ordered 4-layer basic unit repetition was achieved by filament deposition on the thickness-length plane and 3D growth along the width direction. Thus, 3D open-cell structures composed of unit cells with different shapes and dimensions and assembled to form regularly repeated patterns, were obtained. Specimens with ≈ 70% porosity degree, which was the highest porosity achievable without impairing the quality of the specimens (see [18]), were manufactured first. Then, with the aim to study the underlying failure mechanisms of such materials, which according to Gibson and Ashby [8] are on the border between *true cellular solids* and *solids containing isolated pores*, other porosity levels were explored. To do so, in addition to ≈ 70% porosity structures, manufactured using a printer "infill density" parameter of 30%, supplementary structures obtained with "infill density" of 47%, 65%, 82% and 100% were examined. Increasing the "infill density" resulted in a decrease in the space between adjacent filament windings within a single layer of the structures, leading to lower porosity (the 100% "infill density" structure is the least porous one).

Two different notching techniques were examined (Fig. 1(a)). The first one (indicated with Type A) was performed directly during the FDM manufacturing process of the specimen, by printing the bar with a regular thin slot on one edge. Conversely, a sharp notch was introduced after the printing process in the second one (Type B). With regards to Type A, different values of nominal crack length were explored, for specimens with nominal "infill" level of 30% and 100% only. This was realized by imposing incomplete filament deposition in the layers up to the desired notch length. Six different a_0/W ratios uniformly distributed between ≈ 0.2 and ≈ 0.8 were used, so that the morphology of the region ahead of the 3D-printed crack tip remained the same. Regarding Type B, the notch was introduced using a CEAST Notchvis machine, with two sacrificial polyamide-6 bars positioned in such a way to "sandwich" the cellular structure. This resulted in enhanced stability of the cutting process, leading to a higher and more reproducible final quality. The (manual) feeding motion during the cutting process was along the width (that is the layer stacking) direction. Crack length to width ratio, $a_0/W \approx 0.5$ – in agreement with the indications proposed by the reference documents for conducting SE(B) fracture tests on plastics ($0.45 \le a_0/W \le 0.65$) [19–21] – was selected for the five "infill" levels, from 30% to 100%. Special attention was paid to the introduction of notches always in the same position along the length of the specimen, as well as to the obtainment of consistent initial crack length values, so that the crack tip was located always within the same layer. Optical microscopy observations pointed out the notch sharpness – representative of natural cracks in a component – as well as the absence of damage induced by the cutting process ahead of the crack tip for Type B. Further, the consistency provided by the cutting process, as well as the possibility to obtain specific intermediate crack lengths, which are not achievable in Type A due to the fixed pitch imposed by the filament diameter, provided supporting evidences to the choice of Type B as reference method. A dependence of the fracture response on the notch position (in X direction) is expected, as well as on the position of the crack front — both in terms of a_0 value and of the layer intercepted by the crack tip, representative of a specific structure ahead of it.

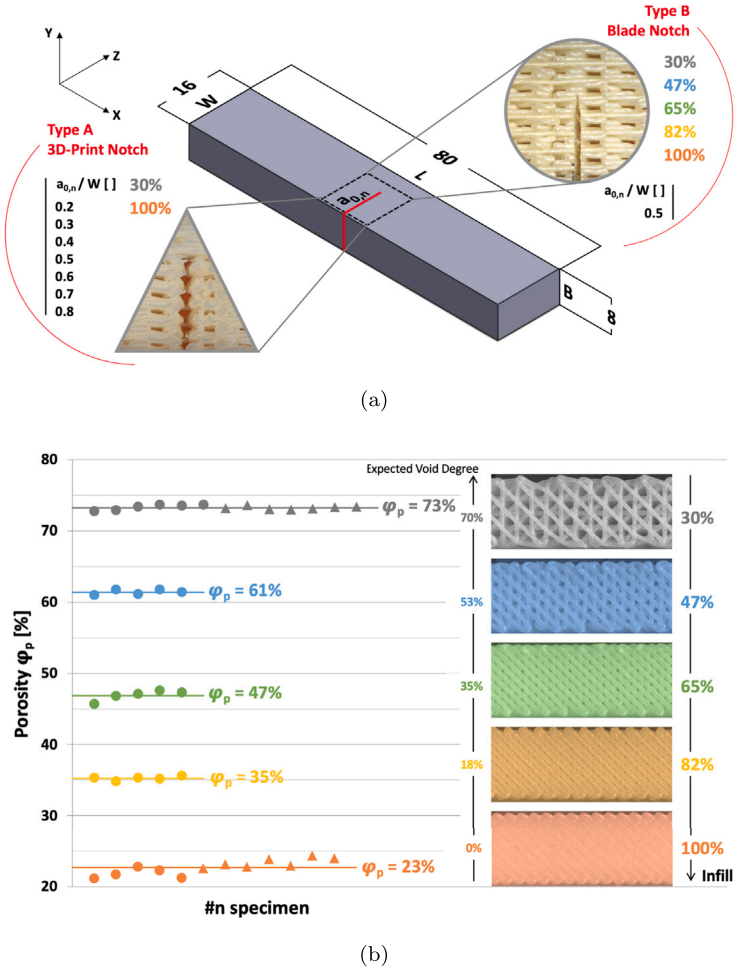

(a)

(b)

Fig. 1. Fracture test specimens with varying nominal “infill” levels (30%, 47%, 65%, 82%, 100%): (a) Geometry of Type A and B specimens. (b) Overview of the pool of specimens tested. For each “infill” level the actual porosity data points (▲ and ● for A and B, respectively) and mean values (lines and adjacent numbers) are indicated. The images of the structures at varying “infill”, taken at the optical microscope, are represented.

2.2. Characterization

2.2.1. Morphological analyses and density measurements

The morphological characterization of the specimens was carried out, at the macro-scale, by means of standard optical and digital microscopy techniques (Leica microscopes, models MS5 and DMS300). These analyses allowed also the assessment of the quality of the samples. As the “infill” level represents the nominal amount of material in each layer, the complement to 100 can be seen as the void degree expected in design phase. For each fracture test specimen, the structure density, ρ_{app}, was determined as the ratio between the specimen mass and its volume. Mass measurements were carried out by means of a digital analytical balance with 10^{-1} mg resolution. The volume was determined from the specimen dimensions, measured using either a digital micrometer (with 1 μm resolution) or a Vernier caliper (with 50 μm resolution), for lengths lower or higher than 20 mm, respectively. This is consistent with the approach adopted for the systems previously studied in compressive conditions [18]. An “apparent” character is attributed to the density of the specimens in consideration of the porous nature of the material. The actual porosity degree of the structures, φ_p, was determined as the complement to 1 of the relative density, $\rho_{rel} = \rho_{app}/\rho_{ABS}$, obtained by normalizing structure and constituent material density data. Thus, 3D-Print pre-notched (Type A) and regular sharp-notched (Type B) specimens were compared, to ensure the compatibility of the outcomes, concerning the sample preparation. Type A and B specimens exhibit very similar porosity levels, which means that even strongly different methods for notch introduction do not affect the final quality of the systems (the contribution of the thin slot to the void degree in Type A specimens was disregarded). Further, by comparing the mean φ_p values calculated over the entire A and B population with the expected void degree (see Fig. 1(b)), differences turned out to increase remarkably in denser systems. The actual porosity levels φ_p span from ≈ 73% (corresponding to the nominal 30% “infill”) to ≈ 22%, which refers to nominal 100% “infill” (Fig. 1(b) and Table 1). Interestingly, in 100% “infill” specimens, the actual mean

Table 1
Specimens tested in fracture tests (with indication of geometry, nominal infill and actual porosity φ_p). The Index of structure elastic stiffness, E_f, is reported for both Type A and B (corresponding to different notching techniques, see text). Fracture toughness at initiation $J_{c,i}$ is reported for Type B specimens (mean value ± standard deviation).

3D Fracture specimens					
Geometry	Infill	Actual φ_p	Type A	Type B	
	[%]	[%]	E_f [a] [MPa]	E_f [b] [MPa]	$J_{c,i}$ [N/mm]
SE(B)	30	73	89 ± 9.9	71 ± 2.6	0.78 ± 0.09
	47	61	–	136 ± 13	0.49 ± 0.05
	65	47	–	279 ± 23	0.66 ± 0.21
	82	35	–	424 ± 15	0.42 ± 0.21
	100	22	1356 ± 80	1201 ± 90	1.23 ± 0.29

[a] : Calculated on specimens with different a_0/W values ($0.3 \leq a_0/W \leq 0.7$).
[b] : Referring to specimens with the same a_0/W value ($a_0/W \approx 0.5$) .

porosity is 22%, rather than the nominal 0% expected. This implies that even the most *continuum*-like systems, manufactured by relying on such FDM machine and filament parameters, present relevant void percentage, that can – and should – not be overlooked. The structures will be referred to by relying on their actual porosity degrees φ_p and according to the chromatic convention used in Fig. 1.

Morphological analyses at the optical digital microscope were carried out on Type B specimens. Both notch position along X direction and crack tip position – always within the same layer – were observed, testifying the consistency and the quality of the notching technique (Fig. 2). Further, measurements of the actual initial crack length (a_0) were performed on the (X,Z) surface of the specimens, to be used in the following FM data elaboration scheme (Fig. 2(a)). Such method was applied for all specimens, for each porosity degree. Further, an additional representative specimen for each φ_p level – not used for testing purposes, yet still considered in the porosity evaluation process, as represented in Fig. 1(b) – was selected and each layer carefully separated by means of a sharp cutter. This step was rigorously performed in order not to modify the layer geometrical features, so that they could be considered representative of the actual filament deposition process, after full separation. For each porosity level, the four layers with different orientations, characteristic of the basic unit, were analyzed at the optical microscope, and the key geometrical parameters were determined *via* image processing software ImageJ. The geometrical features selected as representative were the filament diameter (d, where $d \approx 0.5$ mm), the separation between adjacent windings (D) and their curvature radii (R) (Fig. 2(b)). The key information about the method, applied to the cellular solid case ($\varphi_p = 73\%$), is reported in Fig. 2(b). Both digital microscope analyses and 3D-CAD models from actual part relief clearly highlighted the discontinuous nature of the crack front for all porosity degrees — more evident as higher porosity values are considered (Fig. 2(c)).

2.2.2. Fracture tests

The experimental activity was divided into two phases: phase-1 aimed at setting up the method and facing the experimental and data processing issues; phase-2 specifically dedicated to carrying out fracture tests on systems of different porosity. In phase-1, tests were carried out on the Type A specimens, consisting of two sets, with the lowest and highest porosity degree, respectively, and within each set six test pieces with different a_0/W (Fig. 1(a)). In phase-2, tests were carried out on the Type B specimens, consisting of five sets with different porosity degrees, and within each set, three nominally identical test pieces with $a_0/W = 0.5$. Fracture tests were performed with an Instron test system 3366 (10 kN load cell) equipped with a 3-point bending rig with 10 mm diameter rollers. A span, S, of 64 mm, corresponding to 4 W was used (see Fig. 3(a)). The tests were performed at room temperature, in quasi-static conditions, in displacement control. A crosshead speed, v, of 1 mm/min was selected for the specimens with $a_0/W = 0.5$ – two specimens for Type A and all the specimens for Type B (see Fig. 1(a)) – corresponding to an apparent strain rate of 0.012 min^{-1}. The strain rate was evaluated as

$$\dot{\varepsilon} = \frac{6v(W - a_{0,n})}{S^2} \tag{1}$$

obtained by assuming the specimen as a bar (elastic) characterized by an effective width ($W-a_{0,n}$), where $a_{0,n}$ is the nominal crack length [22]. An “apparent” character is attributed to the strain rate calculated according to Eq. (1), since it is based on the assumption of the absence of stress intensification induced by the notch. For the tests on specimens with different $a_{0,n}/W$ values (in phase-1) v was changed in such a way that $\dot{\varepsilon} = 0.012\ \text{min}^{-1}$ could be obtained. Load *vs.* displacement raw curves were taken as output of the tests. In addition, the tests were video recorded with a digital camera (NIKON D700).

Fracture tests on SE(B) specimens in ductile polymer are extremely prone to be affected by roller penetration (indentation) in the specimen-roller contact areas [20], and this requires a specific *a posteriori* correction procedure be applied to the raw load *vs.* displacement curve coming from the actual fracture test. A correction procedure proposed by ISO13586:2018 [19] and Hale and Ramsteiner [20] requires the execution of an additional experiment on an unnotched specimen with dimensions nominally identical to that tested in the fracture test (a portion of specimen not directly involved in the fracture process can be used as well) using the 3-point bending rig with the minimum span achievable (S = 0 configuration). The porous nature of the cellular systems required special attention in dealing with compliance correction tests, with respect to the case of *continuum*. With the systems here examined,

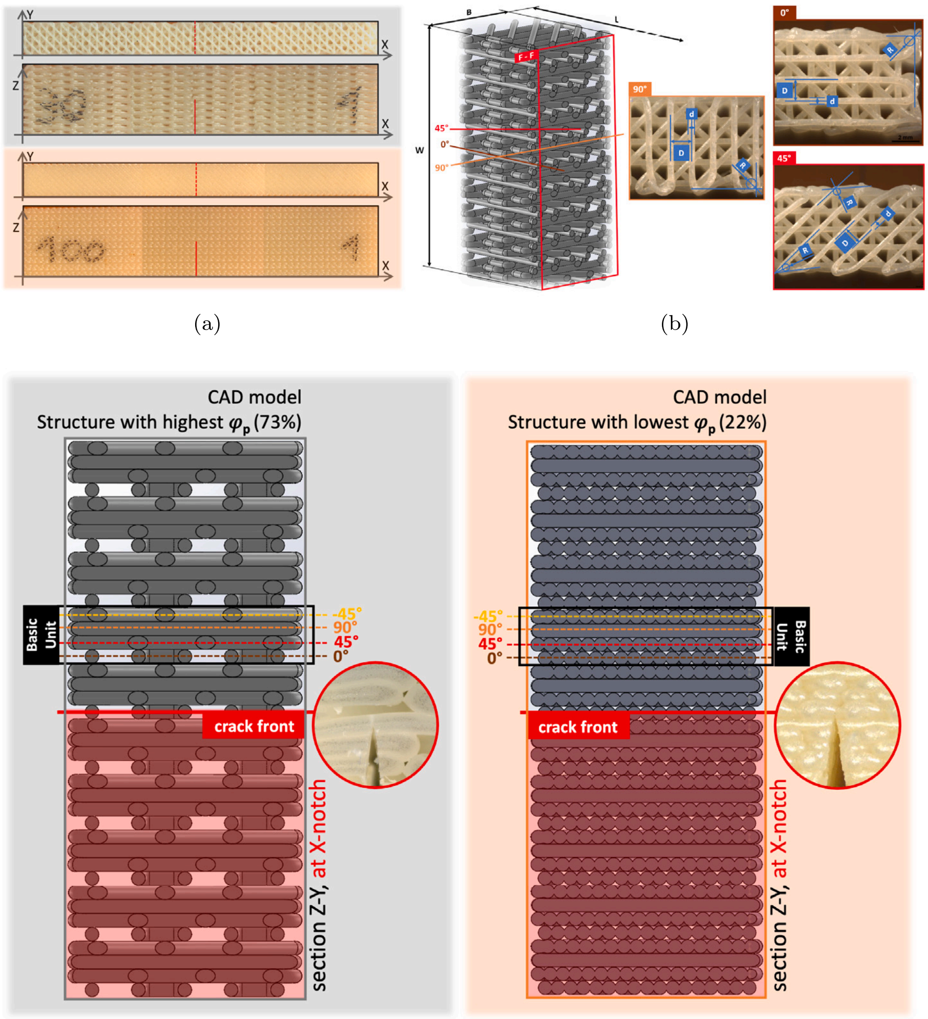

(a) (b)

(c)

Fig. 2. Morphological analyses and notching. (a) Orthogonal views of representative 73% and 22% porosity specimens. Notch position along X direction (X-notch) and length are indicated (red lines). (b) CAD model for φ_p = 73%, with indication of the geometrical parameters (d, D, R, see text). The model view is taken *via* Z-Y section plane F - F, at X-notch. (c) Sections Z-Y at X-notch, with indication of crack front and microscopy images of crack tip.

the local structure of the specimens in correspondence of the top and bottom contact points with the rollers during the fracture test was examined at the optical microscope (red and green asterisks in Figs. 3(a) and 3(c)), and then researched in the side regions of the specimens, far from the notch area and thus not affected by test-induced damage (yellow and light green asterisks in Figs. 3(a) and 3(c)). The correction test was then carried out by positioning the test piece on the rig in such a way to ensure that the local structure in contact with the rollers was the same observed during the fracture test (Fig. 3(b)). The crosshead speed was maintained equal to 1 mm/min for all porosity levels.

Then, to correct the load–displacement curve obtained during the actual fracture test for the indentation effects, the correction curve was subtracted from the actual fracture load–displacement curve. This was performed by subtracting the correction curve displacement from the fracture test displacement at corresponding loads. This procedure was preferred over the one based on the direct use of elastic compliance values (see [19]), by considering that fracture and correction tests showed the fully developed elastic regions at significantly different loads (see Figs. 4(a) and 4(b)). A corrected compliance, indicated with C_0, was determined from this brand-new, load *vs.* corrected displacement, u_{corr}, curve by considering the highest slope linear region. The method was developed in phase-1, and then used in phase-2 for the structures with porosity degrees between 47% and 73%. For the two least porous structures (with porosity of 22% and 35%), the high degree of compactness of the structures prevented from the reliable evaluation of the local patterns, and the correction tests were performed without taking care at the local roller-specimen structure. In phase-2, once the corrected loading curves were constructed for each specimen, for each φ_p, the attention was focused on two parameters: 1. a structure elastic stiffness index, E_f, evaluated directly from C_0; 2. a structure initiation fracture toughness, $J_{c,i}$,

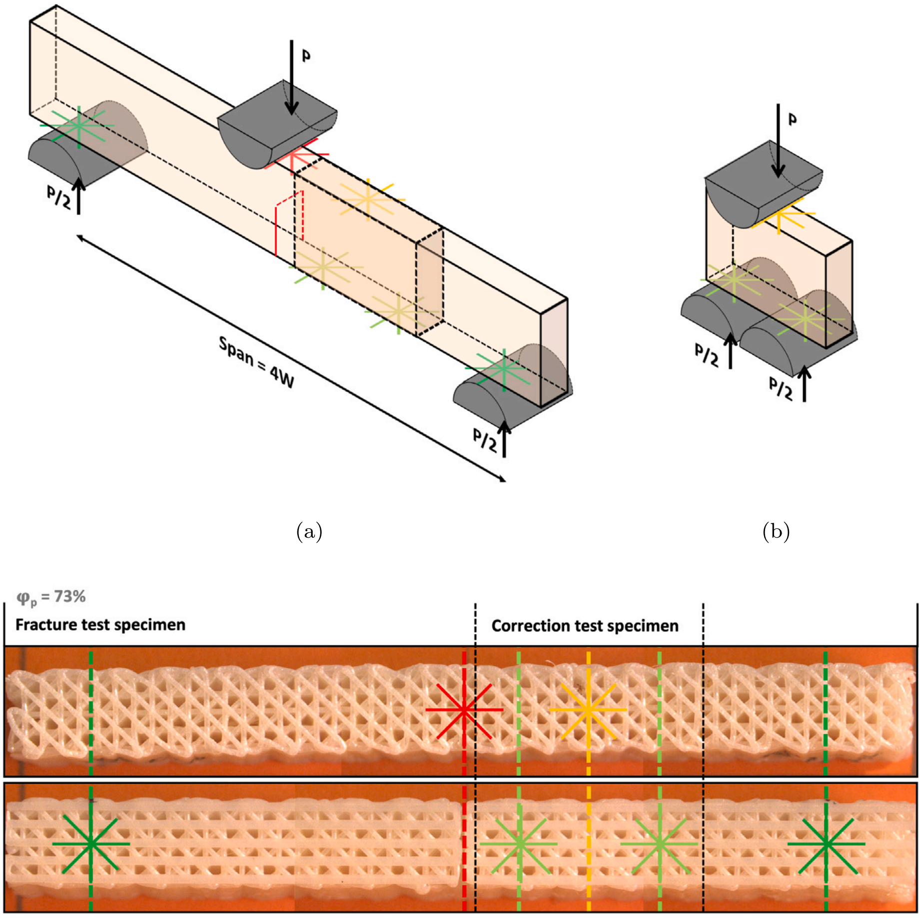

(a) (b)

(c)

Fig. 3. Fracture and correction tests. (a) 3-point bending configuration used in fracture tests on SE(B) specimens; (b) compliance correction test experimental setup; (c) top and bottom (BxW) images of a $\varphi_p = 73\%$ representative specimen used for the structure research phase. Asterisks are used to mark the roller-specimen contact points with the same structure in fracture (red and green) and correction (yellow and light-green) tests (see text).

evaluated in correspondence of the point of fracture initiation. An "apparent" character is attributed to both parameters due to the porous nature of the systems. At low strains, the index of structure elastic stiffness, E_f, is the key parameter. Considering the loading curves, E_f was determined according to the relationship

$$E_f = \frac{2}{B}\frac{f^2}{dC/d\alpha} = \frac{2}{BC}f^2\varphi \tag{2}$$

where $\alpha = a_0/W$, C is the initial mechanical compliance evaluated from the fracture test and $f(\alpha)$ and $\varphi(\alpha)$ are dimensionless purely geometrical functions of α, whose expression for SE(B) specimens tested in 3-pt bending tests with span S = 4W is established in relevant literature about FM of polymeric materials [23]. Under the hypotheses of *continuum*, homogeneity and isotropy, E_f is equal to the Young's modulus, E, in plane stress conditions, and to $E/(1-\nu^2)$, with ν that indicates the Poisson's ratio of the material, in plane strain conditions. However, as the systems under analysis clearly violate all those assumptions, the equivalence between E_f and E is not expected. Then, the attention was mainly focused on the initiation of fracture process. Considering the corrected loading curves, the Fracture Toughness at Initiation $J_{c,i}$ was determined according to the relationship

$$J_{c,i} = \frac{2U}{B(W-a_0)} \tag{3}$$

where U is the area under the P *vs.* u_{corr} curve up to the initiation point. This expression for SE(B) specimens tested in 3-pt bending tests with span S = 4W is established in relevant literature about FM of polymeric materials [20].

Fracture tests were accompanied by high resolution image acquisition (1 image per second), to provide real-time information about the damage phenomena, at least at the macro-scale. Further, from the point of view of data elaboration, a dual approach was followed: the analyses of the loading curves, direct output of the tests, and of the corresponding image sets, were performed

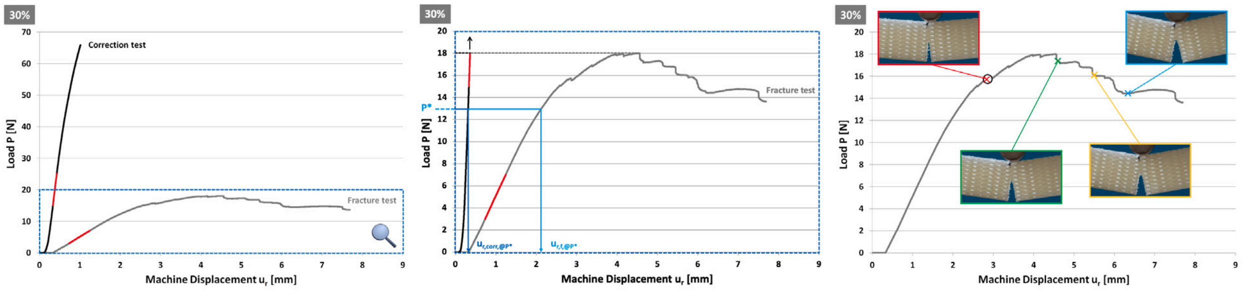

(a) (b) (c)

Fig. 4. Data elaboration procedure for regular sharp-notched specimens (Type B). (a) Raw loading curves from fracture and correction test (representative $\varphi_p = 73\%$ specimen). The initial linear elastic regions are indicated in red. (b) Procedure of displacement identification at same load level (P*). (c) Correlation between camera images and loading curve analysis in correspondence of morphological and structural changes.

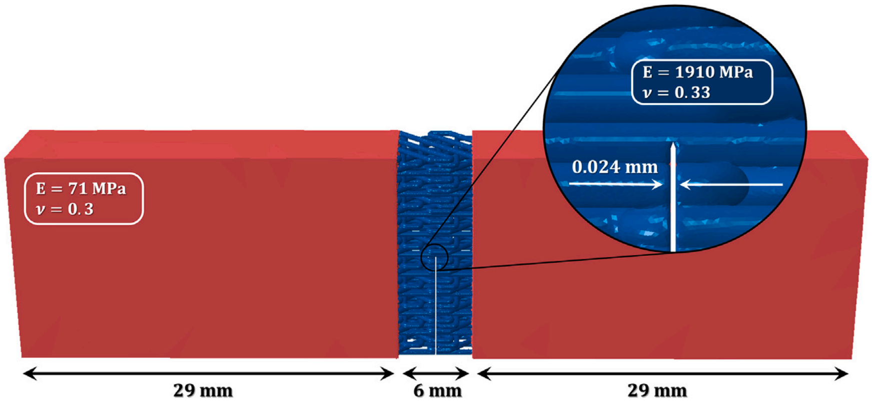

Fig. 5. FEM model beam: in garnet, *continuum* equivalent material and, in blue, 3D-structured material (with values of elastic modulus, E, and Poisson's ratio, ν). The detail of the notch is represented in the magnification circle, and its width indicated.

separately, to avoid mutual influence of the outcomes during the elaboration phase. A preliminary qualitative analysis was started, by identifying the peaks of the curves, as they might be correlated with some kind of damage occurring in the structure. The nature of such damage could not be directly inferred, however the peaks' height was regarded as a potential indicator about the underlying mechanisms (filament decohesion or crack propagation), as well as provide information about damage magnitude. Then, the analysis of high-resolution images taken during the tests was performed, by detecting both morphological changes in the structures and eventual crack propagation. The frames where such variations took place were selected and then correlated with the corresponding data points on the loading curves. A good result agreement was found between the two independent strategies. Further, camera images analysis allowed to provide meaning to load drops, by discriminating between filament relative movements and decohesion and actual crack propagation. Thus, it was possible to place the fracture process initiation, (○ in Fig. 4(c)). The entire procedure was repeated for all the specimens tested.

2.3. Computational model

A computational model of a representative specimen with $\varphi_p = 73\%$ was implemented. For a cost-effective computational approach, the whole specimen was divided in three distinct regions (Fig. 5). A homogeneous linear elastic isotropic material – characterized by a macroscopic elastic modulus – was assigned to the two external regions. Thus, all dissipative phenomena were assumed to take place in the central region, where fracture initiation and crack propagation phenomena are expected to take place.

In order to create the central region of the domain, a representative volume element with size 6x8x16 mm^3 was extracted from the CAD model, converted in STL file and eventually imported in Gmsh [24] to be meshed. The 3D-structure was meshed with linear tetrahedral elements having a characteristic size of 0.03 mm increasing up to 0.1 mm far from the notch. A coarser mesh was used for the external parts, using the same type of elements. A 0.024 mm wide notch was introduced in the 3D-structure through a boolean operation. Notch position and length replicate the experimental ones. Only the 3D-structured central region of the beam was modeled (6 mm wide). At the interfaces between the *continuum* end parts and the 3D-structured central region, the nodes are shared, thereby no contact strategy was implemented. The external regions were modeled as an isotropic linear elastic material, with an effective Young's modulus of 71 MPa [18], an effective Poisson's ratio of 0.3 and an apparent density consistent with the experimental value

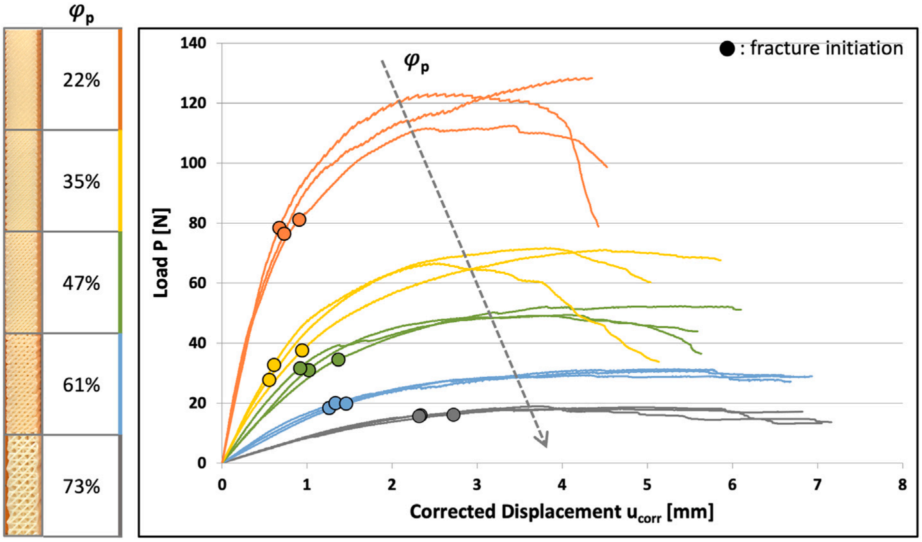

Fig. 6. Load, P, *vs.* Corrected Displacement, u_{corr}, curves of specimens with different φ_p (22%, 35%, 47%, 61%, 73%). For each specimen, the point of fracture initiation is indicated (●).

measured for this structure (see Table 1). The equivalent macroscopic elastic modulus was determined through the post process of the linear range of the experimental tests on the same samples. The 3D-structure was modeled as a von Mises elastic–plastic material, with Young's modulus and yield stress equal to those measured on the filament (*i.e.*, 1910 MPa and 36.2 MPa, respectively [18]) and Poisson's ratio assumed equal to 0.33. The filament density (1.06 g/cm^3) was used. A slight linear isotropic work hardening was defined for numerical purposes. The numerical simulation was performed by solving the dynamic equation through an explicit solver (ABAQUS/Explicit). The displacement was applied on the nodes belonging to the center of the 3D-structure to replicate the action of the loading roller of the experimental apparatus. The displacement was imposed through a sigmoidal shaped function of time, providing a smooth loading condition and minimizing accelerations. The displacement boundary conditions were imposed to simulate the three-point bending experimental setup. The bottom extreme edges of the beam were constrained imposing a zero displacement along the load direction. On one of these edges was imposed a null displacement along the direction of the beam and a further node was constrained to eliminate rigid body motions. The fracture initiation was modeled through a "ductile damage", defined through the equivalent fracture strain at damage initiation (0.02), the stress triaxiality factor (−0.33, representative of a uniaxial state of stress) and the equivalent plastic strain rate (0 s^{-1}). An exponential softening of the material was implemented based on an initiation fracture toughness (critical energy release rate) value equal to 3.09 N/mm. In order to make the simulation computationally efficient, a fixed mass scaling was imposed (the time increment was fixed to 10^{-6} s, and the density was scaled accordingly). The quasi-static loading condition was achieved verifying that the kinetic energy was less than the 5% of the internal energy. A mass proportional damping, equal to 100 s^{-1}, was applied to reduce the numerical oscillations. The equivalent plastic strain, $\bar{e}$, was used for visualization purposes to identify the elements which underwent high plastic strains. Specifically, $\bar{e}$ is defined as

$$\bar{e} = \int_0^T \sqrt{\frac{2}{3}\left(\underline{\underline{\dot{\varepsilon}}}^p : \underline{\underline{\dot{\varepsilon}}}^p\right)}\, dt \tag{4}$$

where $\underline{\underline{\dot{\varepsilon}}}^p$ is the incremental plastic strain tensor and " : " the double inner product operator. Thereby, $\bar{e}$ is a scalar value that for an uniaxial tension state corresponds to the highest principal plastic strain.

3. Results and discussion

The Load, P, *vs.* corrected displacement, u_{corr}, curves of the specimens tested in phase-2 are reported in Fig. 6. The effect of φ_p is clearly evident, as increasing the porosity degree led to lower loads and initial stiffness values. The fracture initiation point was placed by relying on the evaluation of both the loading curves and the digital images taken during the tests. The curves-images synergistic approach proved that fracture initiation took place in correspondence of discontinuities in loading curves, sometimes in the form of full-fledged load drops, sometimes as significant slope variations. It is worth underlining that delamination phenomena – which, at various level, characterize the fracture propagation phase – were not noticed prior to fracture initiation. In consideration of this outcome, in the elaboration of the experimental data, the attention was focused on the initiation point and on the region preceding it.

The effect of porosity, φ_p, on the index of structure elastic stiffness, E_f, was studied on sharp-notched Type B specimens (● in Fig. 7(a)). At first, it clearly emerges that the a_0/W values resulting from the blade notching phase are consistent, both within and

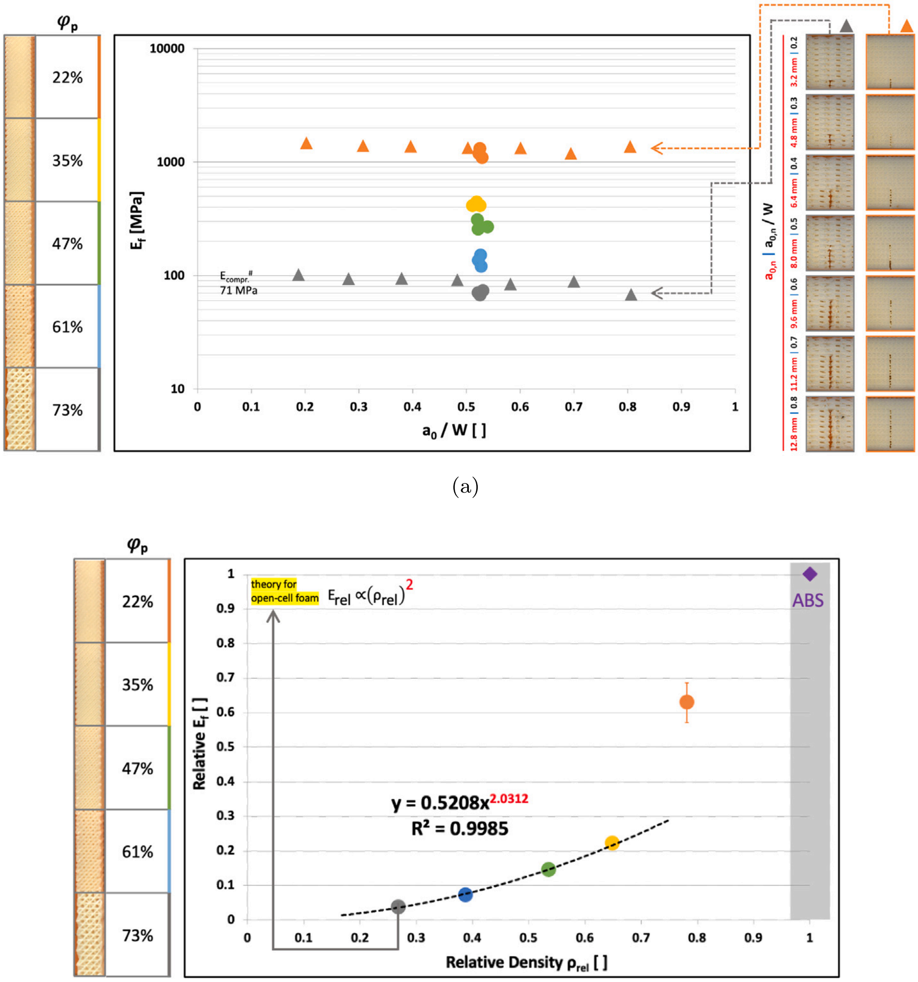

(a)

(b)

Fig. 7. Structure elastic stiffness, E_f, at varying φ_p (22%, 35%, 47%, 61%, 73%). (a) E_f, *vs.* normalized crack length, a0/W, for Type B (●, identical nominal a_0/W) and A (▲, variable a_0/W ($0.2 \le a_0/W \le 0.8$, φ_p = 22% and 73%). (b) Relative E_f *vs.* relative density, ρ_{rel}. The *continuum* data point, characterized by unitary value in relative properties, is represented as limit case for cellular materials (◆). Standard deviation bands are indicated. A power-law best fit (black dashed line) is forced on data points in the range 35% ≤ φ_p ≤ 73%, according to the theory for open-cell foams [8].

between the porosity levels. Further, as expected, E_f is strongly dependent on φ_p, assuming higher values as lower porosity levels are considered. E_f values within the same φ_p set turned out to be similar, and the results were reported in Table 1, expressed as mean value ± standard deviation. In addition, the effect of a_0/W ratio on E_f was studied on 3D-print-notched Type A specimens. In such scenario, the data refer only to φ_p levels of 22% and 73% (▲ in Fig. 7(a)). The corresponding images of the notch region – taken at the optical microscope – together with a_0 and a_0/W values, are also reported. It is important to point out that the E_f values are representative of the true structure elastic stiffness of the systems, after applying the compliance correction procedure described above. A relevant indentation effect was recorded for both highly-compliant 73% and stiffer 22% porosity systems, causing at least a 20% underestimation in the value of E_f, if not properly corrected. By considering the corrected data showed in Fig. 7(a), E_f assumes an almost constant value over a wide range of initial crack length ($0.3 \le a_0/W \le 0.7$), leaving apart the extremes of the explored range, where boundary effects might be significant.

Mean values and standard deviations are reported in Table 1. By comparing the E_f values obtained from Type A and Type B specimens (for φ_p levels of 22% and 73%, respectively), a general agreement can be observed. A comparison between E_f and the Young's modulus, E, determined under compression [18] can be made. It emerges that, in spite of the complex nature of the systems, E_f and E assume the same value (71 MPa).

The index of structure elastic stiffness of regular sharp-notched specimens (Type B) was studied as a function of the porosity degree of the systems. Following the classical approach proposed in [8] and widely established in relevant literature about cellular materials, the results were represented in relative terms. More specifically, relative E_f was determined by normalizing E_f with E_{ABS}

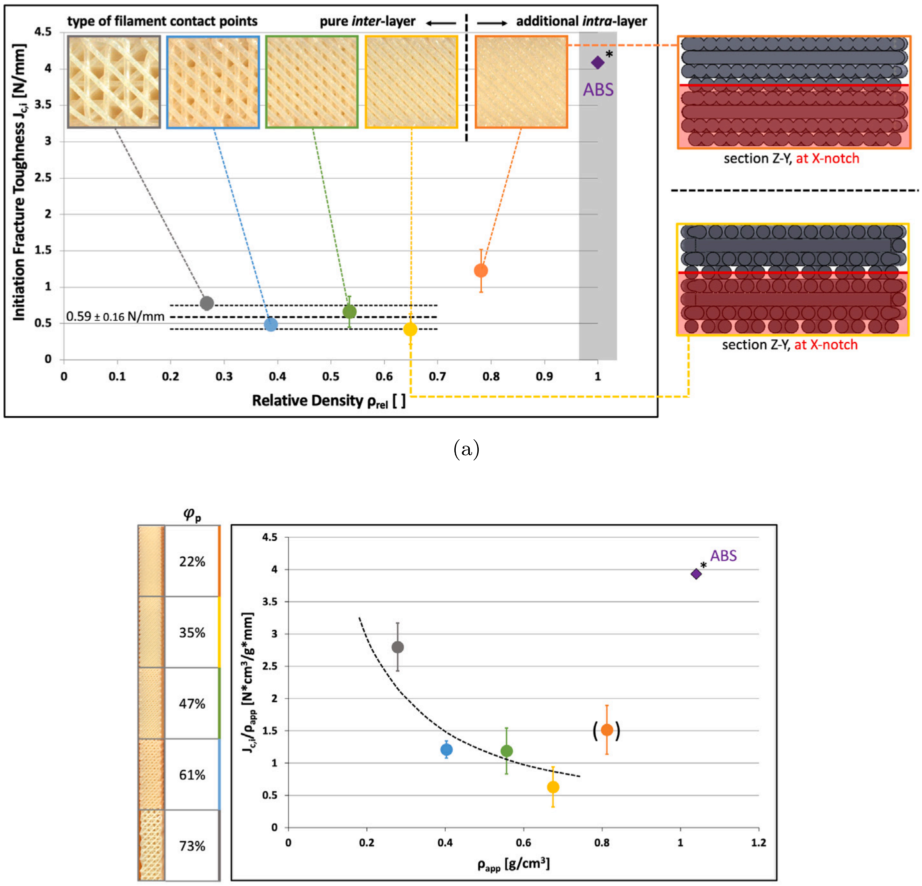

(a)

(b)

Fig. 8. Fracture toughness at initiation, $J_{c,i}$, at varying φ_p (22%, 35%, 47%, 61%, 73%). (a) $J_{c,i}$ *vs.* Relative Density, ρ_{rel} (●). The *continuum* case is also represented (◆*, see text). Mean ± standard deviation forced on 35% ≤ φ_p ≤ 73% data points are indicated (black lines and corresponding values). Images representing filament connectivity, either just *inter*- or both *inter*- and *intra*-layer — are reported. (b) Normalized Fracture Toughness *vs.* Apparent Density, ρ_{app}.

— calculated from tensile tests on the extruded filament and equal to 1910 MPa [18], while relative density ρ_{rel} is defined as the complement to 1 of the porosity degree φ_p. The results were expressed as mean values ± standard deviation, and represented in Fig. 7(b). It clearly emerges that a unique power-law trend fits well the experimental data with the only exception represented by the least porous system, which significantly deviates, suggesting the presence of different underlying mechanisms governing the response. Such outcome could be explained by hypothesizing a transition region when reaching conditions close to *continuum*-like configuration. Further, the exponent value of the power-law fitting equation (= 2.03) is consistent with the theory for open cell foams in compressive conditions (= 2), developed in [8]. This suggests that the theoretical model is able to correctly predict the response of the systems not only in borderline porosity conditions (*i.e.* for φ_p = 73%) but also outside of the range for the classical definition of cellular materials (*i.e.* for φ_p < 70%).

The Fracture Toughness at Initiation $J_{c,i}$ – determined according to Eq. (3) – is plotted against the relative density, ρ_{rel}, in Fig. 8 (● indicator). Data were reported as mean values, accompanied by the corresponding standard deviation bands. It is worth noting that, in Fig. 8 (as well as in Figs. 10 and 11), the data point (◆ indicator) corresponding to a non-porous industrial ABS grade ($J_{I,c}$ value from [25]) was added as a reference (*continuum*).

The initiation fracture toughness of the systems is almost constant over a wide range of porosity levels (from 35% to 73%), taking into account the experimental uncertainties of the data, thus resulting independent on the cell size of the structures. $J_{c,i,mean}$ – expressed as mean value ± standard deviation and calculated as the mean of the mean values obtained for each porosity level – resulted of 0.59 ± 0.16 N/mm. Interestingly, as already pointed out for E_f, data for 22% porosity specimens (relative density equal to 0.78, orange indicator) were not aligned, assuming far higher values, indeed. Such outcome was regarded as a further indication of the presence of a transition region when *continuum*-like conditions were approached. In search of evidences supporting this hypothesis, the structure of the architected systems was analyzed, with special attention paid to the zone interested by the fracture process. More specifically, it was observed that filament junctions were limited to *inter*-layer type in specimens with φ_p ≥ 35%: thus, the junction points where contact between filaments was established were between two consecutive layers only. On the

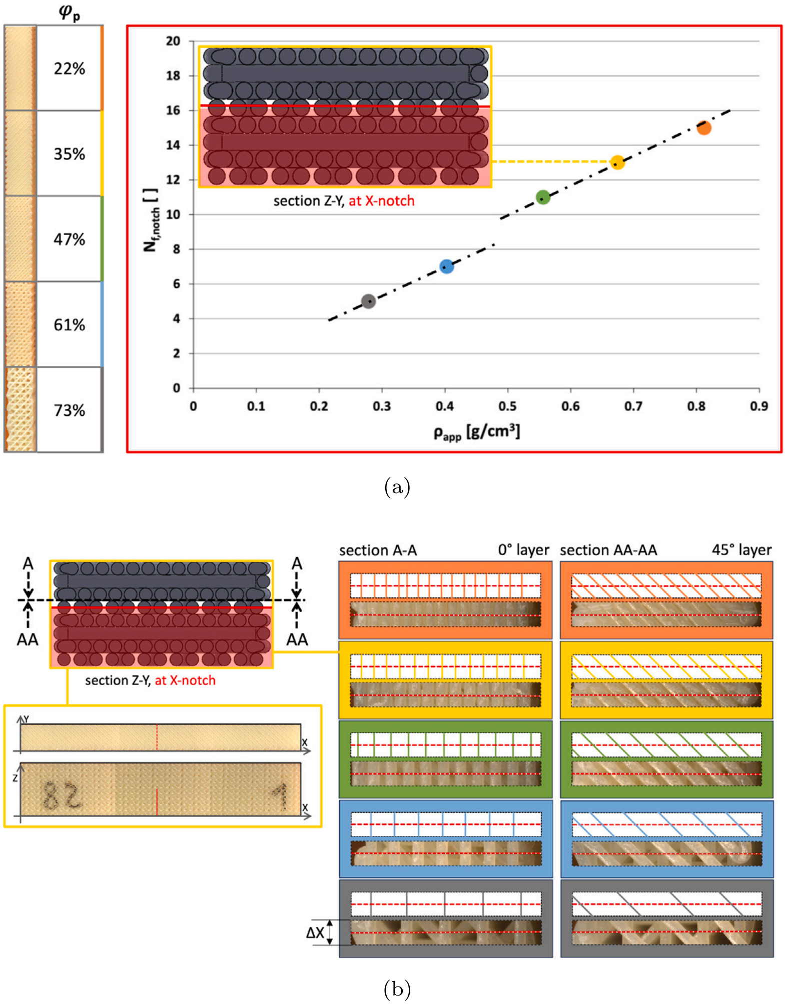

Fig. 9. Macro-structural analyses at varying φ_p (22%, 35%, 47%, 61%, 73%). (a) Relationship between the number of filaments constituting the notch front, $N_{f,notch}$, and the Apparent Density, ρ_{app} (black dashed lines). (b) Contact points between the filaments of 0° and 45° layer ahead of the notch front, within $\Delta X = 2d$ (see text). Images of Section A-A and AA-AA, at X-notch (red dashed line), as well as the position and orientation of the generatrix line for each filament (colored lines), are represented.

contrary, further analyses on the least porous structure ($\varphi_p = 22\%$) at the optical microscope pointed out the presence of *intra*-layer type junctions, in addition to the *inter*-layer previously discussed. For this system, the infill level imposed during the design phase was so high that consecutive windings of filament within the same layer touch themselves, regardless of their orientation: thus, additional filament contact surfaces, with far larger extension in comparison with the still present *inter*-layer contribution, were obtained in this structure.

This clearly emerges from the sections of the 3D-CAD models of the structures (Fig. 8(a)) at the notch position. The discontinuous nature of crack front was no longer valid in 22% porosity structure, where contact and occasionally superposition between *intra*-layer adjacent filament windings was detected by optical microscopy analyses and then reported in the CAD model. Thus, in this specific scenario, the crack front can be seen as “quasi-continuous”, at least as close as possible to the *continuum* case.

By plotting the initiation fracture toughness, $J_{c,i}$, of the various structures, normalized over the corresponding apparent density, ρ_{app}, against the apparent density (in Fig. 8(b)), a decreasing trend is observed as φ_p decreases from 73% to 35% (again, the least porous structure deviates from this trend). Fig. 9(a) provides an important help in interpreting this result. It shows the relationship, constructed relying on both microscopy analyses and 3D-CAD models, between the number of filaments constituting the crack front in the 0° layer, $N_{f,notch}$, and the structure apparent density ρ_{app}. A bi-linear dependence, characterized by two traits sharing the same slope, with the shift between $\varphi_p = 47\%$ and 61% being related to the discrete nature of $N_{f,notch}$ ($N_{f,notch} \in \mathbb{N}$), clearly comes out. In consideration of this, from Fig. 8(b) it emerges that, by keeping the least porous structure apart, the contribution in resisting fracture given by each filament constituting the crack front is less effective as φ_p decreases. To explain this result, tentative (macro-)structure/property relationships were researched, by means of morphological analyses on a representative specimen for each

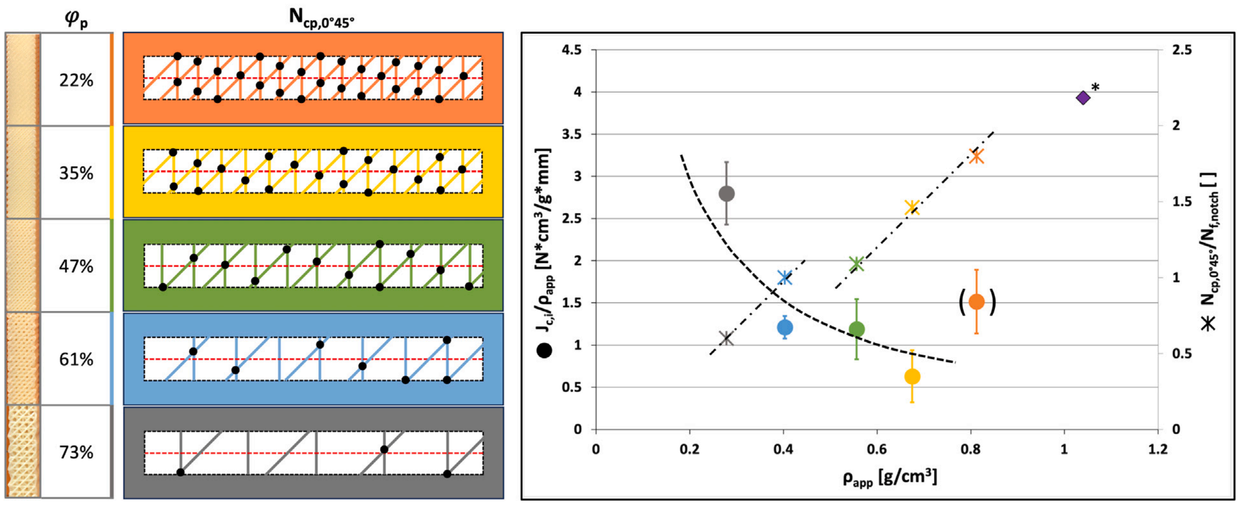

(a)

(b)

Fig. 10. Structure–property relationships: Effect of mechanical constraint at varying φ_p (22%, 35%, 47%, 61%, 73%). (a) Determination of the number of contact points between the filaments of 0° and 45° layers, $N_{cp,0°45°}$. (b) Fracture Toughness at Initiation per unit of Apparent Density $J_{c,i}/\rho_{app}$ (●) and number of contact points per filament constituting the discontinuous notch front $N_{cp,0°45°}/N_{f,notch}$ (✱) *vs.* ρ_{app}. The *continuum* case is also represented (◆*, see text).

porosity degree considered. More specifically, being interested in the notch front zone (where the fracture process zone develops during fracture), the evaluation of the number of contact points between the filaments in the 0° layer (which contains the notch tip) and those in adjacent layer (at +45°, which is involved in subsequent crack propagation) was attempted. A region of interest characterized by width twice the actual filament diameter d ($\Delta X \approx 2d$) along the X-direction, was selected. For each φ_p, the actual macro-structure of the 0° and +45° layers was defined by means of generatrix lines, representative of position and orientation of each filament involved (see Fig. 9(b)). By merging the generatrix lines, the actual contact points between 0° and +45° could be detected, and their number $N_{cp,0°45°}$ recorded (Fig. 10(a)). Then, $N_{cp,0°45°}$ – which characterizes the systems' architecture ahead of the crack tip – was normalized over $N_{f,notch}$, in order to obtain the number of contact points per filament constituting the discontinuous crack front. Such parameter – whose dependency on ρ_{app} is showed in Fig. 10(b), where data of $J_{c,i}/\rho_{app}$ are also reported to facilitate understanding – can be considered as an index of the degree of mechanical constraint experienced by each single filament constituting the crack tip, at different porosity levels. The response can be seen as governed by two competing mechanisms: on the one hand, an increase in ρ_{app} means a higher number of filament involved in the definition of the crack front and contributing to resist and delay crack propagation, leading to an improvement in the initiation fracture toughness; on the other hand, however, the rising number of filaments results in a reduction in their mobility – and thus in their ability to bear the imposed strains – as a result of the higher constraint generated, leading to increased local rigidity and lowering the fracture toughness at initiation. Thus, the constancy of $J_{c,i}$ in the porosity range $35\% \leq \varphi_p \leq 73\%$ can now be seen the result of the coexistence of opposing mechanisms — which either promote or undermine the fracture toughness at initiation.

Finally, as both the index of structure elastic stiffness and the fracture toughness at initiation resulted to be strongly influenced by the apparent density of the systems, their dependency in normalized form ($J_{c,i}/\rho_{app}$ *vs.* E_f/ρ_{app}) was studied (Fig. 11). The results suggest a U-shaped trend at varying porosity levels, with the minimum locating between 22% and 35% porosity — closer to the latter. Thus, while being characterized by significantly different specific stiffnesses, the normalized fracture toughness values for 22% turned out to be equivalent to those coming from 47% and 62%. Indeed, the 73% porosity structures (the only properly defined as full-fledged cellular materials) proved to be even tougher, in specific terms, demonstrating once more why highly-porous Architected Cellular Materials (ACMs) are so interesting from both a scientific and industrial point of view.

The experimental analysis focused on the initiation of the fracture process, with the crack propagation phase set aside. The possibility to investigate this phase *via* a FEM approach was explored (Fig. 12). The load *vs.* displacement response obtained through the numerical simulation is reported in Fig. 12(a) along with the three experimental curves obtained on the specimens of the same type ($\varphi_p = 73\%$).

The numerical simulation predicted reasonably well the experimental load *vs.* displacement response, by taking into account the variability of the experimental response observed for the three different specimens examined. This suggests a high fidelity of the predicted failure mechanisms, as well as a confirmation of the reliability of the intrinsic fracture energy value of the bulk material used. It is worth underlining that an initiation fracture toughness value of 3.09 N/mm is consistent with that expected for an ABS

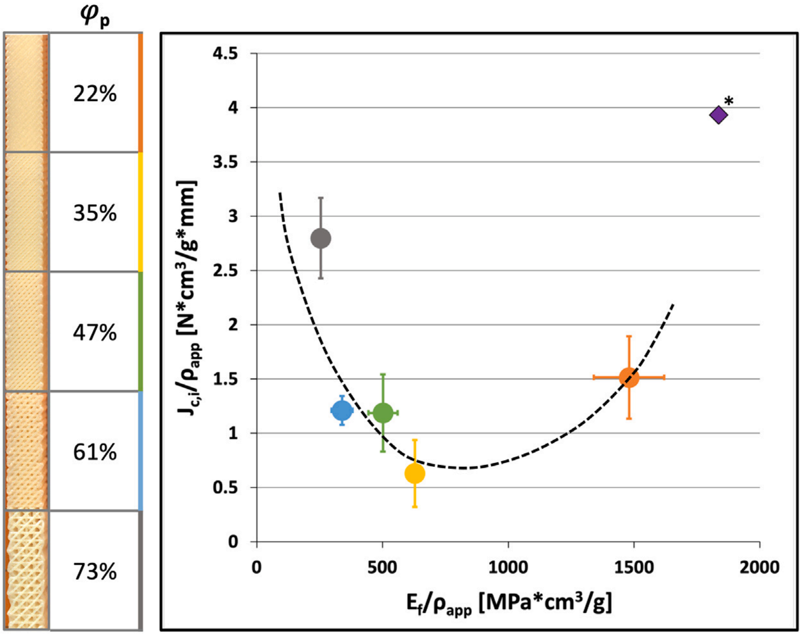

Fig. 11. Normalized fracture toughness at initiation, $J_{c,i}/\rho_{app}$, *vs.* Normalized Index of structure elastic stiffness, E_f/ρ_{app}, (●) for varying φ_p (22%, 35%, 47%, 61%, 73%). Standard deviation bands are reported for both properties. A qualitative trend of the data points – except for the *continuum* case (◆*) – is proposed (black dashed line).

resin, in consideration of the difficulties encountered in its experimental determination (see [25,26]). In Figs. 12(b)–12(d), the spatial distribution of the equivalent plastic strain, $\bar{e}$, defined according to Eq. (4), at three different displacement levels is represented. It emerges that two major failure phenomena take place during the fracture process: (i) high stretching of the filaments aligned along the X-direction and located at the crack tip (0° layer) and (ii) shear delamination at the interface between two adjacent layers above the crack tip. A threshold value of 0.32, corresponding to the strain at break of the ABS filament in uniaxial tensile tests [18], is used in the color scale as a reference. Another minor failure was observed from FEM simulation, consisting in local permanent deformation in the region of the applied load (figure not showed). This can be ascribed to roller-specimen indentation effects due to the high compliance of the structure. This evidence was also observed experimentally, proving the importance of the compliance correction tests (see Section 2.2.2).

4. Conclusions

In this work, ABS open-celled cellular model structures with controlled architecture (based on the repetition of an ordered 4-layer basic unit) were manufactured by FDM, and their fracture behavior investigated under the framework of FM (mode-I loading). Structures with different degrees of porosity ($\varphi_p = 22\% \div 73\%$) were examined. They shared the same beam-like structural element arrangement, properly scaled according to the structure porosity.

From SE(B) tests on specimens with different a_0/W ratios, chosen in such a way that the ligament resulted composed of multiples of the 4-layer basic unit, the possibility to describe the small strain response by means of a single parameter (a structure elastic stiffness index, E_f) was clearly pointed out. For the most porous structure, E_f resulted very similar to the Young's modulus measured from compression tests. Further, for a given a_0/W ratio, E_f turned out to be very slightly affected by the geometrical characteristics of the notch tip (sharpness degree), varied by using two different specimen notching techniques. By considering the results from the sharp notched specimens, a power-law type dependence on the structure apparent density was observed for E_f (with the exponent in very good agreement with the theoretical one proposed in the relevant literature for open-cell foams). Only the least porous structure ($\varphi_p = 22\%$) clearly deviated from this trend. This outcome, coupled with the experimental observation of intra-layer filament junctions establishing only for $\varphi_p = 22\%$ in addition to the inter-layer ones common to all the porosity levels, suggested the existence of a transition, for $\varphi_p < 35\%$, from the behavior of a *true cellular solid* to that of a *solid containing isolated pores*.

The initiation fracture toughness ($J_{c,i}$) data, from tests on sharp notched specimens, seem to support this hypothesis. $J_{c,i}$ for $\varphi_p = 22\%$ showed a clear upward deviation if compared to the data coming from the structures with higher porosity, practically characterized by the same toughness (if the standard deviation of the results is taken into account). The fact that no toughness increase was observed by decreasing the structure porosity from $\varphi_p = 73\%$ to $\varphi_p = 35\%$, has been tentatively ascribed to the

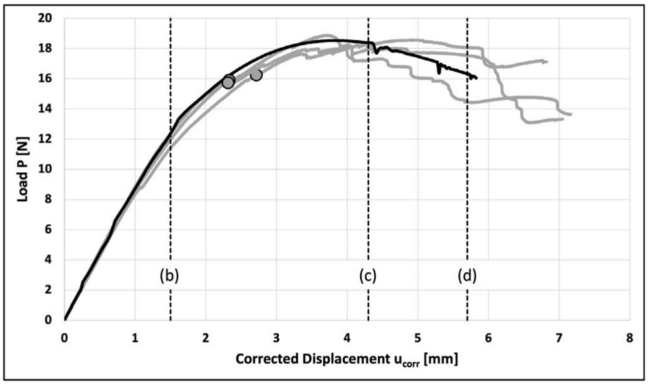

(a) Loading curves

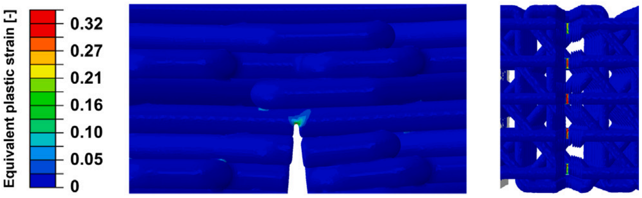

(b) $u_{corr} = 1.5$ mm

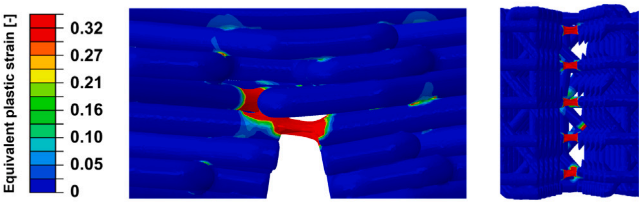

(c) $u_{corr} = 4.3$ mm

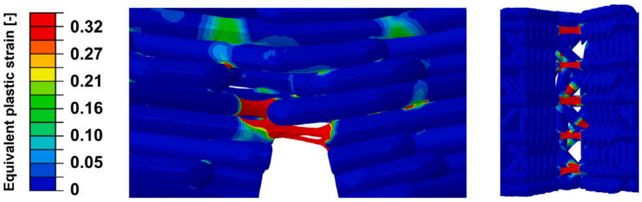

(d) $u_{corr} = 5.7$ mm

Fig. 12. FEM analysis on the $\varphi_p = 73\%$ structure. (a) Load *vs.* Displacement curves: comparison between the experimental tests (grey, with fracture initiation point indicated with ●) and the computational model (black); (b-c-d) Equivalent plastic strain fields at different levels of u_{corr} (side and bottom view).

macro-confinement action experienced by the filaments constituting the discontinuous crack front, able to reduce the effectiveness of each single filament in resisting fracture.

The finite element simulations have shown their potential to enlighten the deformation mechanisms of the complex 3D-architecture examined and the progression of the material damage. The developed numerical model can be further employed to predict the overall toughness of 3D-structures with different porosity degrees and even architectural arrangements.

CRediT authorship contribution statement

Jacopo Agnelli: Conceptualization, Data curation, Investigation, Methodology, Writing – original draft. **Claudia Pagano:** Conceptualization, Investigation, Methodology, Supervision, Writing – review & editing. **Irene Fassi:** Investigation, Resources. **Luca**

D'Andrea: Data curation, Investigation, Methodology, Writing – original draft. **Pasquale Vena:** Conceptualization, Investigation, Methodology, Writing – review & editing. **Laura Treccani:** Resources, Investigation. **Fabio Bignotti:** Investigation, Resources. **Francesco Baldi:** Conceptualization, Funding acquisition, Investigation, Methodology, Supervision, Writing – review & editing.

Funding

Financed by the European Union - NextGenerationEU (National Sustainable Mobility Center CN00000023, Italian Ministry of University and Research Decree n. 1033 - 17/06/2022, Spoke 11 - Innovative Materials & Lightweighting). The opinions expressed are those of the authors only and should not be considered as representative of the European Union or the European Commission's official position. Neither the European Union nor the European Commission can be held responsible for them [CUP: D83C22000690001].

Declaration of competing interest

The authors declare the following financial interests/personal relationships which may be considered as potential competing interests: Francesco Baldi reports financial support was provided by European Union. If there are other authors, they declare that they have no known competing financial interests or personal relationships that could have appeared to influence the work reported in this paper.

Acknowledgments

The authors are grateful to Fabbrica d'Armi Pietro Beretta S.p.A. (Gardone Val Trompia, Brescia, Italy), Industrie Polieco-M.P.B. S.r.l. (Cazzago San Martino, Brescia, Italy) and Bioteck S.p.A. (Arcugnano, Vicenza, Italy) for the support kindly provided. A special thanks to Michelangelo Conter, student at University of Brescia, Italy, for the CAD models.

Data availability

Data will be made available on request.

References

[1] Ligon SC, Liska R, Stampfl J, Gurr M, Mülhaupt R. Polymers for 3D printing and customized additive manufacturing. Chem Rev 2017;117:10212–90. http://dx.doi.org/10.1021/acs.chemrev.7b00074.
[2] Penumakala PK, Santo J, Thomas A. A critical review on the fused deposition modeling of thermoplastic polymer composites. Compos Part B: Eng 2020;201:108336. http://dx.doi.org/10.1016/j.compositesb.2020.108336.
[3] Volpe V, Lanzillo S, Affinita G, Villacci B, Macchiarolo I, Pantani R. Lightweight high-performance polymer composite for automotive applications. Polymers 2019;11:1–16. http://dx.doi.org/10.3390/polym11020326.
[4] Mohammadi H, Ahmad Z, Mazlan SA, Aidy M, Johari F, Siebert G, Petr M, Saeid S, Koloor R. Lightweight glass fiber-reinforced polymer composite for automotive bumper applications: A review. Polymers 2023;15:1–30.
[5] Dyer WE, Kumru B. Polymers as aerospace structural components: how to reach sustainability? Macromol Chem Phys 2023;224:1–25. http://dx.doi.org/10.1002/macp.202300186.
[6] Najmon JC, Jacob DJ, Wood ZM, Tovar A. Cellular helmet liner design through bio-inspired structures and topology optimization of compliant mechanism lattices. SAE Int J Transp Saf 2018;6:217–35. http://dx.doi.org/10.4271/2018-01-1057.
[7] Kussmaul R, Biedermann M, Pappas GA, Jónasson JG, Winiger P, Zogg M, Türk DA, Meboldt M, Ermanni P. Individualized lightweight structures for biomedical applications using additive manufacturing and carbon fiber patched composites. Des Sci 2019;5:1–24. http://dx.doi.org/10.1017/dsj.2019.19.
[8] Gibson LJ, Ashby MF. Cellular solids: structure and properties. 2nd ed.. Cambridge University Press; 1997, http://dx.doi.org/10.1017/CBO9781139878326.
[9] Fleck NA, Deshpande VS, Ashby MF. Micro-architectured materials : past, present and future. Proc R Soc A 2010;466:2495–516. http://dx.doi.org/10.1098/rspa.2010.0215.
[10] Schaedler TA, Carter WB. Architected cellular materials. Annu Rev Mater Res 2016;46:187–210. http://dx.doi.org/10.1146/annurev-matsci-070115-031624.
[11] Benedetti M, Plessis A, Ritchie RO, Dallago M, Razavi SMJ, Berto F. Architected cellular materials : A review on their mechanical properties towards fatigue-tolerant design and fabrication. Mater Sci Eng R 2021;144:100606. http://dx.doi.org/10.1016/j.mser.2021.100606.
[12] Anderson T. Fracture mechanics : fundamentals and applications. CRC Press; 2017, http://dx.doi.org/10.1201/9781315370293.
[13] Patterson BM, Kuettner L, Shear T, Henderson K, Herman MJ, Ionita A, Chawla N, Williams J, Sun T, Fezzaa K, Xiao X, Welch C. Synchrotron CT imaging of lattice structures with engineered defects. J Mater Sci 2020;55:11353–66. http://dx.doi.org/10.1007/s10853-020-04840-y.
[14] Chen E, Luan S, Gaitanaros S. On the compressive strength of brittle lattice metamaterials. Int J Solids Struct 2022;257:111871. http://dx.doi.org/10.1016/j.ijsolstr.2022.111871.
[15] Feng Y, Huang T, Gong Y, Jia P. Materials & design stiffness optimization design for TPMS architected cellular materials. Mater Des 2022;222:111078. http://dx.doi.org/10.1016/j.matdes.2022.111078.
[16] Seiler PE, Tankasala HC, Fleck NA. The role of defects in dictating the strength of brittle honeycombs made by rapid prototyping. Acta Mater 2019;171:190–200. http://dx.doi.org/10.1016/j.actamat.2019.03.036.
[17] Luan S, Chen E, Gaitanaros S. Energy-based fracture mechanics of brittle lattice materials. J Mech Phys Solids 2022;169:105093. http://dx.doi.org/10.1016/j.jmps.2022.105093.
[18] Agnelli J, Pagano C, Fassi I, Treccani L, Bignotti F, Baldi F. Mechanical behaviour of ductile polymer cellular model structures manufactured by FDM. Mech Mater 2024;190:104882. http://dx.doi.org/10.1016/j.mechmat.2023.104882.
[19] ISO13586:2018. Plastics — Determination of fracture toughness (GIC and KIC) — Linear elastic fracture mechanics (LEFM) approach.
[20] Hale G, Ramsteiner F. A testing protocol for conducting J-crack growth resistance curve tests on plastics. In: Fracture mechanics testing methods for polymers adhesives and composites. 2001, p. 140–57.

[21] ASTMD6068:2018. Standard test method for determining J-R curves of plastic materials.

[22] Gosch A, Arbeiter FJ, Agnelli S, Berer M, Pinter G, Baldi F. J-testing of polymers via the load separation criterion based ESIS TC4 procedure: Effect of the specimen size. Polym Test 2020;89:106637. http://dx.doi.org/10.1016/j.polymertesting.2020.106637.

[23] Williams JG. Kc and gc at slow speeds for polymers. In: Fracture mechanics testing methods for polymers adhesives and composites. 2001, p. 11–26.

[24] Geuzaine C, Remacle JF. Gmsh: A 3-D finite element mesh generator with built-in pre- and post-processing facilities. Internat J Numer Methods Engrg 2009;79:1309–31. http://dx.doi.org/10.1002/nme.2579.

[25] Baldi F, Agnelli S, Andena L, Blackman BRK, Castellani L, Frontini PM, Kučera J, Laiarinandrasana L, Pegoretti A, Salazar A, Warnet L. Determination of the fracture resistance of ductile polymers : The ESIS TC4 recent experience. Mater Perform Charact 2020;9:675–87. http://dx.doi.org/10.1520/MPC20190175.

[26] Baldi F, Agnelli S, Riccò T. On the determination of the point of fracture initiation by the load separation criterion in J-testing of ductile polymers. Polym Test 2013;32:1326–33. http://dx.doi.org/10.1016/j.polymertesting.2013.08.007.